Study of morphology of aerosol aggregates formed during co-pyrolysis of C_3H_8+$Fe(CO)_5$

N A Ivanova[1], A A Onischuk[1], S di Stasio[2], A M Baklanov[1] and G A Makhov[1]

[1] Institute of Chemical Kinetics and Combustion SB RAS, 630090, Novosibirsk, Russia
[2] Istituto Motori CNR Aerosol and Nanostructures Laboratory, Via Marconi 8, 80125 Napoli, Italy

E-mail: ivanova@ns.kinetics.nsc.ru

Abstract

Formation of aerosol nanoparticles as well as carbon nanotubes and nanofilaments is studied during co-pyrolysis of iron pentacarbonyl and propane with argon as a carrier gas in a flow reactor. Gaseous intermediates from propane thermal decomposition (CH_4, C_2H_6 and C_3H_4) and $Fe(CO)_5$ conversion are monitored by gas chromatography and IR-spectroscopy, respectively. The aerosol morphology is studied by transmission electron microscopy (TEM) and high resolution TEM. The aerosol particle concentration and size distribution are measured by an automated diffusion battery. The crystal phase composition of particles is studied by x-ray diffractometry. The decomposition of the $Fe(CO)_5$ + Ar mixture resulted in an iron aggregate formation composed of fine primary particles. In the case of lower pyrolysis temperatures, about 450 K, the primary particle mean diameter is about 10 nm, and consequently, the majority of the primary particles are superparamagnetic, thus forming compact aggregates. At intermediate pyrolysis temperatures in the range 800–1040 K the primary particle diameter is about 20–30 nm, and most of the particles are ferromagnetic in nature. The coagulation of these particles results in a chain-like aggregate formation. Finally, at temperatures higher than the Curie point (1043 K) the ferromagnetic properties vanish and the formation of compact aggregates is observed again. The co-pyrolysis of $Fe(CO)_5$ and C_3H_8 mixed with Ar carrier gas resulted in aerosol aggregate structures dramatically different from those formed by iron pentacarbonyl pyrolysis. In particular, in the temperature range 1070–1280 K, we observed Fe_3C particles connected by long carbon nanotubes (CNTs). The aggregate morphology is described in terms of a fractal-like dimension D_f, which is determined from TEM images on the basis of a scaling power law linking the aggregate mass (M) and radius (R), $M \sim R^{D_f}$. The Fe_3C–CNT aggregate morphology is a function of the inlet ratio between propane and iron pentacarbonyl concentrations $[C_3H_8]_0/[Fe(CO)_5]_0$. At the low ratio of $[C_3H_8]_0/[Fe(CO)_5]_0 < 80$ the fractal dimension of aggregates decreases (from 1.7 down to about 1) with the increasing ratio of inlet concentrations. This effect, as observed by TEM, is due to the increase in the mean nanotube length. Vice versa, in the range $C_3H_8]_0/[Fe(CO)_5]_0 > 80$ the fractal aggregate dimension is higher for a larger ratio of $[C_3H_8]_0/[Fe(CO)_5]_0$, which is explained by the larger thickness of growing nanotubes obtained for a relatively large propane concentration. The aggregate formation mechanism includes consecutive stages of iron aggregate formation due to $Fe(CO)_5$ decomposition, carbon deposition on iron particles from C_3H_8 pyrolysis intermediates, carbon dissolution in iron particles, nanotube nucleation at the carbon concentration of about 60 at.% in Fe–C solution and disruption of the Fe–C aggregates into small pieces by the growing nanotubes.

1. Introduction

Pyrolysis and combustion of hydrocarbons are typical soot forming processes. Soot particles are a hazardous source of atmospheric pollution [1]. The toxicity of such aerosol particles is related to their size and morphology [2]. In particular, it is known that the soot chain-like aggregates can adsorb the semivolatile organic compounds more efficiently than compact aggregates [3]. Soot particles (or aggregates of particles) of size $\sim 1\,\mu$m can penetrate and remain in the alveolar regions of human lungs resulting in mutagenic and carcinogenic effects [4]. Both the lung penetration and macrophage clearance depend essentially on the aerosol aggregate structure [5]. Thus, the study of morphology of the soot aerosol aggregates formed during the hydrocarbon pyrolysis and combustion is of current importance. Soot aggregate morphology is controlled by different factors such as humidity (which leads to a restructuring of the aggregates to compact structures [6]), high temperature (which causes soot aggregate restructuring in the flame [7]) and electric charge, which can affect the morphology at the stage of cluster–cluster aggregation [8, 9] and govern the aggregate restructuring [10].

Basic flame synthesis and pyrolysis of hydrocarbons can be used in combination with the addition of organometallic precursors (containing Co, Ni, Fe) in order to induce dramatic changes in the morphology of the generated carbon aerosol nanoparticles. In particular, these routes may be used for the synthesis of carbon nanotubes (CNTs) and carbon nanofibres (CNFs) [11–16,20]. These structures represent a new important class of technological materials that have numerous novel and useful properties [17–19]. The transport properties, coagulation rate constant and the specific surface area for this kind of aerosols can change significantly with a small variation of the synthesis conditions. During the last decade CNTs and CNFs have come under a toxicology scrutiny [21, 22]. The ability of long and thin fibres to reach the gas-exchange region of the lungs gives rise to anxiety in the scientific society. The lung penetration efficiency depends both on the length and shape [23]. The CNT and CNF aerosol if inhaled can cause such types of pathology as fibrosis, pleural changes and mesothelioma [22,24–26] as well as oxidative stress in cells [27–29]. Furthermore, the transition metals, used as precursors in a hycrocarbon mixture, are included as constituents of the CNT and CNF aerosol and, therefore, may contribute to the oxidative–induced inflammation and toxicity [23].

As a consequence of the points outlined above, the relevance of studies concerned with the evolution of nanostructure and morphology occurring during the formation of hybrid carbon–metal nanoaerosols is apparent.

This work investigates the morphology of aerosol aggregates obtained in a flow reactor by a co-pyrolysis of propane with iron pentacarbonyl diluted in argon, which is a typical system for CNT generation. Besides, the interest in Fe(CO)$_5$ is caused by its efficient use as a fire suppressant in hydrocarbon flames [30, 31].

The decomposition of Fe(CO)$_5$ diluted in argon is a sub-process of the C$_3$H$_8$ + Fe(CO)$_5$ + Ar pyrolysis and the comprehension of this step is crucial to the understanding of the final aerosol formation. A few papers in the literature

to date are focused on the study of morphology and size aerosol aggregates formed during the Fe(CO)$_5$ pyrolysis or combustion. Several decades ago Beischer and Winkel [32] investigated the correlation of temperature and iron aggregate morphology. They found experimentally that open structure chain-like iron aggregates are formed at temperatures lower than the Curie point and vice versa, rather than compact aggregates with highest temperatures. They proposed a model of chain-like aggregate formation, which could take into account the magnetic interactions between primary particles. In the 1980s, Kasper and co-workers [33] studied the formation of compact and linear aggregates of iron oxide (Fe$_2$O$_3$) under combustion of Fe(CO)$_5$ and the mobility and aerodynamic aggregate diameters were determined [34–36]. More recently, other authors studied the formation of iron oxide particles generated under laser pyrolysis of Fe(CO)$_5$ [37] and thermal decomposition of Fe(CO)$_5$ in a flow reactor [38]. Unfortunately, the major part of the foregoing papers was devoted to the analysis of iron oxide particles and there is a lack of knowledge about the mechanism of Fe particle formation during the pyrolysis of the iron containing precursors.

The objective of this paper is to study the complex topic of aerosol particle formation from the pyrolysis of C$_3$H$_8$ + Fe(CO)$_5$ mixtures, including the eventual changes in aerosol size, nanostructure and morphology occurring during the whole process. This complex phenomenology is comprehensive in understanding the mechanisms of iron aggregates' formation (Fe(CO)$_5$ + Ar pyrolysis), Fe–C aggregate formation and carbon nanotube nucleation (C$_3$H$_8$ + Fe(CO)$_5$ + Ar pyrolysis).

2. Experimental

A schematic diagram of the experimental apparatus is shown in figure 1. The thermal decomposition was carried out at atmospheric pressure in a quartz horizontal flow reactor with an inner diameter of 3.0 cm equipped with a coaxial oven. The mixtures of Fe(CO)$_5$ + Ar and C$_3$H$_8$ + Ar were prepared beforehand and stored in high pressure gas cylinders. The inlet mole fractions of propane and iron pentacarbonyl were varied from 0 to 7.6×10^{-3} and from 0 to 1.4×10^{-4}, respectively. Almost all the experiments were performed at the same value of flow rate. Thus, further in the text, if not mentioned especially, the flow rate was 8 cm^3 s^{-1} at STP. The reactor was operated at temperatures in the range 440–1280 K, which corresponded to residence times in the reaction zone $\tau = 10.5$ s to 5.1 s, respectively.

At the exit of the reactor both gaseous by-products and aerosol particles were sampled for analysis. The concentrations of CO and Fe(CO)$_5$ vapours were measured by an IR-spectrometer Bruker Vector 22. Gas chromatography was used to determine the concentration of gaseous intermediates from propane pyrolysis as well as propane conversion. Identification of the species was accomplished by matching the gas-chromatographic retention times to pure gas standards.

The size and morphology of aerosol particles were observed by a transmission electron microscope (TEM) JEM-100SX and a high resolution transmission electron microscope (HRTEM) JEM-2010. The samples for TEM and HRTEM
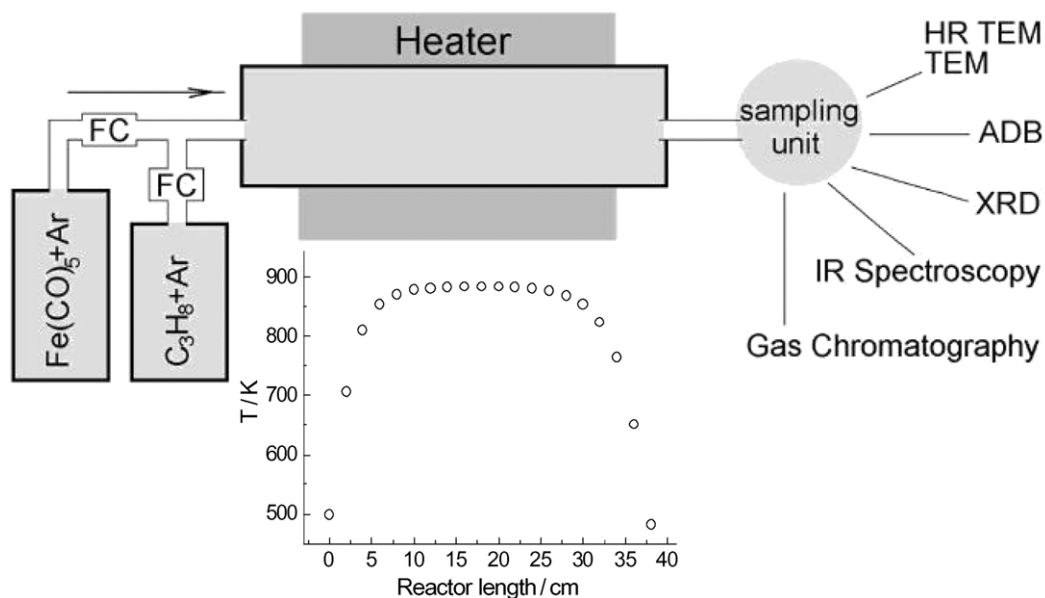
Figure 1. Schematic diagram of experimental apparatus. FC—flow rate control unit.
(This figure is in colour only in the electronic version)

were obtained by thermophoretical precipitation on standard
(3 mm diameter) copper grids covered by the polyvinylformvar
or the carbon support film. Aerosol concentration and size
distribution at room temperature were monitored [39–41] by
an automated diffusion battery (ADB) spectrometer, coupled
with a condensation chamber (CC) and a condensation nucleus
counter (CNC). The crystal phase analysis of particles was
carried out by a URD-63 diffractometer using CuK_α radiation.
X-ray diffraction (XRD) samples were obtained directly by the
deposition of aerosol particles onto a high efficiency aerosol
filter.

3. Results

3.1. Iron aerosol aggregate formation under $Fe(CO)_5+Ar$ pyrolysis

The iron pentacarbonyl pyrolysis was carried out as follows.
First, the quartz reactor was carefully cleaned. Thereafter,
the reaction mixture $Fe(CO)_5$ plus Ar was supplied at the
inlet section of the reactor. The outlet concentrations of
$Fe(CO)_5$ and CO (reaction product) were monitored during
a few hours of reactor run. The concentration of iron
pentacarbonyl $[Fe(CO)_5]$ was observed to decrease and that
of CO to increase, respectively, with respect to increase in
the reactor runtime t_W until both concentrations settled at a
stationary level (figure 2). This increase in the conversion
degree is probably related to the fact that both homogeneous
and heterogeneous (wall reaction) decompositions of iron
pentacarbonyl occur. The walls are activated during the
reaction because of iron deposition, resulting in an increase
in the heterogeneous decomposition rate. In this paper we
consider only the experiments with the activated wall reactor,
i.e. when the conversion has become steady at a stationary
level. Figure 3 shows the conversion of iron pentacarbonyl
versus residence time, which was measured by changing
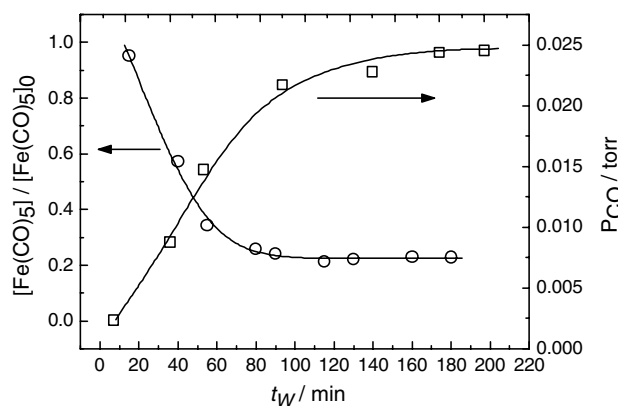the feeding flow rate at the reactor input. Figure 4 reports

Figure 2. The output $Fe(CO)_5$ and CO (right) concentration versus
the laboratory reaction time (t_W). Inlet molar fraction is
$[Fe(CO)_5]_0 = 6.5 \times 10^{-6}$, pyrolysis temperature $T = 463$ K.

the conversion degree measured as a function of reaction
temperature corresponding to different inlet concentrations
$[Fe(CO)_5]_0$. These results demonstrate that higher $[Fe(CO)_5]_0$
corresponds to a lower conversion ratio $[Fe(CO)_5]/[Fe(CO)_5]_0$.

Aerosol particles collected from the reactor outlet on
copper grids were observed by TEM. The nature of such
an aerosol was of aggregates composed of smaller particles,
which are normally referred to in the literature as *primary*
particles. The aggregate shape and size were found to depend
significantly upon the reactor temperature. For example,
at a low operating pyrolysis temperature $T < 510$ K the
iron aggregates were observed to be compact (figure 5(*a*)).
In the range of middle temperatures 510 to 1040 K the
aggregates were formed in a chain-like shape (figure 5(*b*)).
At temperatures higher than 1040 K the compact aggregates
were observed again (figure 5(*c*)). The mean diameter d of
primary particles, as determined by HRTEM, was found to
increase from about 10 nm at $T = 445$ K to about 30 nm at
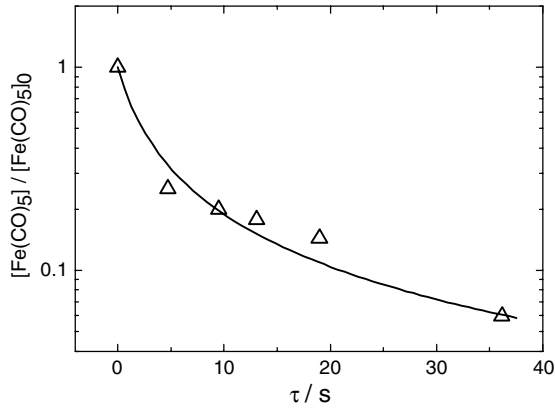$T = 1173$ K (figure 6). The equivalent geometric radius R of

2073

Figure 3. The output Fe(CO)$_5$ concentration versus the residence time (τ). Inlet molar fraction of Fe(CO)$_5$ is 6.5×10^{-6}, pyrolysis temperature $T = 473$ K.
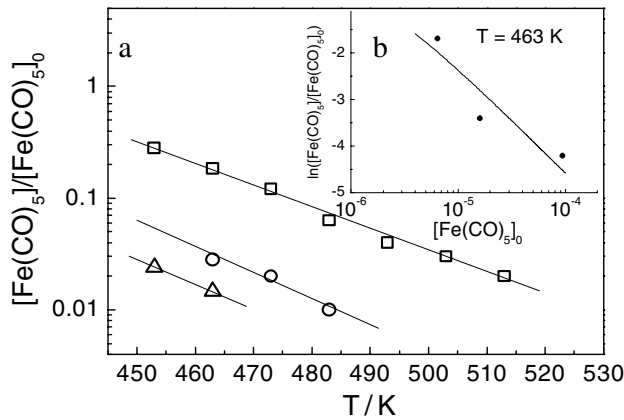

Figure 4. (*a*) The output Fe(CO)$_5$ concentration versus the pyrolysis temperature. Inlet molar fraction of Fe(CO)$_5$: [Fe(CO)$_5$]$_0$ = 6.5×10^{-6} (squares), 1.6×10^{-5} (circles) and 9.5×10^{-5} (triangles). Solid lines are guides to the eye. Inset (*b*) shows the output Fe(CO)$_5$ relative concentration versus the inlet Fe(CO)$_5$ molar fraction for $T = 463$ K. Solid line corresponds to equation (6).

iron aggregates was determined from TEM images according to a procedure described in detail elsewhere [42] from the following equation:

$$R = \frac{1}{2}\sqrt{LW}, \tag{1}$$

where L and W are the dimensions of the smallest rectangle enclosing the 2D image of the aggregate.

The mean arithmetic radius and the number concentration of iron aggregates at the reactor outlet are shown versus the pyrolysis temperature in figure 7. In the temperature range 450 to 580 K a contemporary decrease in the number concentration and increase in aggregate radius with temperature are observed. Further, in the range $T > 600$ K, the mean radius R decreases and the number concentration is independent of T. TEM image elaboration (by measuring particle volumes) showed that the aerosol mass concentration did not change with temperature at $T > 600$ K, i.e. the decrease in R in figure 7(*a*) is actually due to the change of aggregate shape.

The aggregate morphology here is quantitatively described in terms of the fractal-like dimension D_f, which can
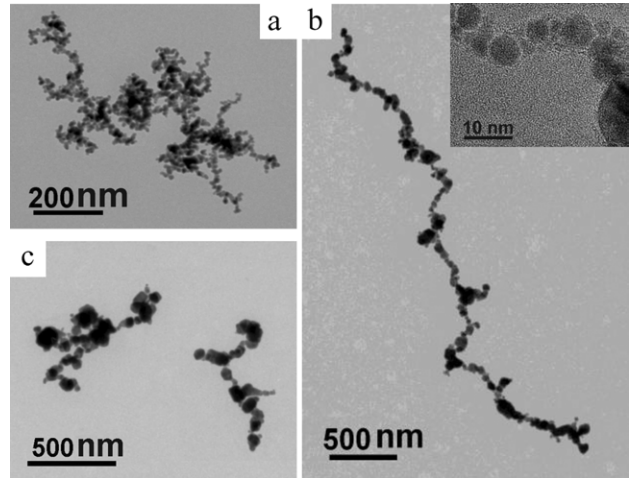
Figure 5. TEM images of iron aggregates formed at pyrolysis of Fe(CO)$_5$+Ar. Inlet molar fraction is [Fe(CO)$_5$]$_0$ = 9.5×10^{-5}, pyrolysis temperature $T = 573$ K (*a*), 873 K (*b*), 1173 K (*c*). The inset of picture 'b' is HRTEM image of iron primary particles inside an aerosol aggregate.
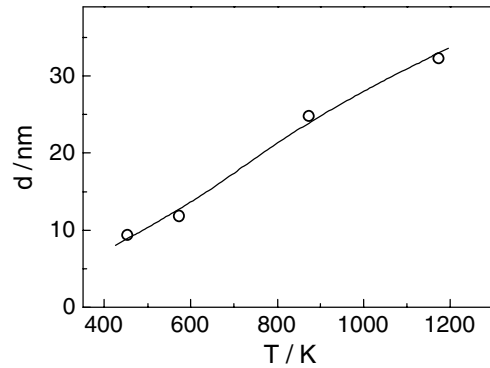

Figure 6. Mean arithmetic diameter of primary particles of iron aggregates versus the pyrolysis temperature. Inlet molar fraction is [Fe(CO)$_5$]$_0$ = 9.5×10^{-5}.

be determined from a power relation between the aggregate mass M and radius [43]:

$$M \propto R^{D_f}. \tag{2}$$

We use two procedures for TEM image processing in order to determine the mass M of each aggregate. The first procedure consists of the measurement of the integral density of individual aggregate as the sum of the grey values of all the pixels which constituted the aggregate image. A correction to the background density was also done. It is assumed that the local grey density in the aggregate image is proportional to the local thickness of the original aggregate. Therefore, the mass of the original aggregate is considered to be proportional to the integral density of the aggregate image. This approach seems to be reasonable because it is known that even the fractal-like dimension of the 2D projection is approximately equal to the D_f value of the original 3D object if $D_f < 2$ [43, 44]. Figure 8 shows a typical plot of log M versus log R. Each point corresponds to a single aggregate.

The second procedure consists of the estimation of the volume of each aggregate from the TEM image. Each
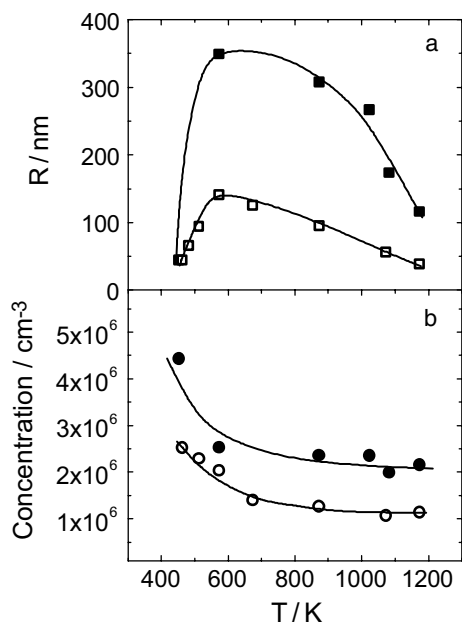
Figure 7. Mean arithmetic radius (R) (a) and number concentration (b) of iron aggregates versus the pyrolysis temperature. Initial molar fraction of Fe(CO)$_5$ - 9.5×10^{-5} (solid symbols) and 6.5×10^{-6} (open symbols). Circles are ADB data, squares—TEM image elaboration results.
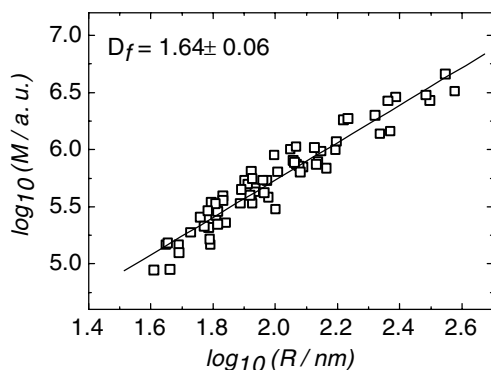

Figure 8. The $\log(M)$ versus $\log(R)$; M is iron aggregate mass and R is iron aggregate radius, inlet molar fraction of Fe(CO)$_5$ is [Fe(CO)$_5$]$_0$ = 9.5×10^{-5}, the pyrolysis temperature $T = 1173$ K. Iron aggregate mass (in arbitrary units) was determined by measurement of the integral density of individual aggregate TEM image. The solid line corresponds to $D_f = 1.64$.

aggregate image is partitioned into constituting blocks. Each block is approximated by a sphere or a cylinder. In some cases, the size of each block is equal to the size of a primary particle, whereas in some other cases each block corresponds to a group of closely adjacent primary particles. On the basis of the estimation for aggregate volume we obtain the value of aggregate mass through the density of primary particles $\rho = 7.8$ g cm^{-3}. A power law regression of the data points allows us to write equation (2) in the following form:

$$M(g) = 5.0 \times 10^{-14}[R(\mu m)]^{D_f}, \qquad (3)$$

Equation (3) is valid in the whole experimental range of reaction temperatures and Fe(CO)$_5$ inlet concentrations.
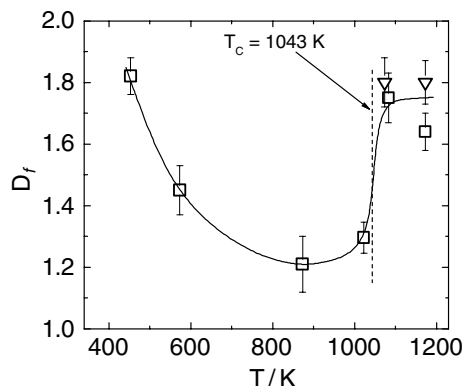

Figure 9. Fractal-like dimension (D_f) of iron aggregates versus the pyrolysis temperature; T_C—Curie point; the inlet molar fraction of Fe(CO)$_5$ is [Fe(CO)$_5$]$_0$ = 9.5×10^{-5}.

Both the image processing procedures described above return the same value of fractal-like dimension. The results described quantitatively in figure 5 can now be expressed in a quantitative form through the fractal dimension and are shown versus the pyrolysis temperature T in figure 9. Thus at T below about 500 K we retrieve compact aggregates with D_f about 1.7–1.8 that correspond to the case shown in figure 5(a). Similarly with T in the range 500 to 1040 K, D_f is found to decrease from 1.6 to 1.2 with increasing temperature, which is the case shown in figure 5(b). And at temperatures higher than about 1040 K fractal dimension is relatively large again being 1.6–1.8, as previously shown in figure 5(c). This behaviour of D_f is probably related to the temperature dependence of the primary particle diameter (see figure 6). In the temperature range from 450 to 570 K the mean size of primary particles was less than 15 nm. These particles are mostly superparamagnetic [48]. There are no long-range interactions between these particles, and aggregates are formed by the diffusion limited cluster–cluster aggregation (DLCA) mechanism. It is well known that DLCA results in $D_f = 1.7$–1.8 [42,49–51]. On the other hand, at temperatures from 570 to 1040 K the mean size of primary particles was 15–30 nm and the majority of particles is ferromagnetic [48]. Thus, there were long-range interactions between these particles during the aggregate formation resulting in the low values of $D_f = 1.2$–1.5 [52–54]. At the range $T > 1040$ K the fractal-like dimension was measured to be about 1.7. At temperatures higher than the Curie point $T_C = 1043$ K iron particles are paramagnetic, and the aggregation is governed again by the DLCA mechanism resulting in $D_f \approx 1.7$.

The XRD analysis of aerosol aggregates sampled on aerosol filters is performed to detect crystal phase composition. XRD patterns of aggregates sampled at $T = 1173$ K show picks of BCC iron and FeO (figure 10, curve 1). The measured values of the lattice constant for BCC iron are equal to 2.871(1) Å, which is larger by 1% than that for pure iron ($a_{(BCC-Fe)} = 2.866$ Å) [45]. The possible reason for such a lattice parameter deviation for iron is the influence of dissolved interstitial atoms (such as C, O). FeO can be a product of the passivation by oxygen from air before the XRD analysis [46]. An example of the same XRD analysis performed at $T = 1173$ K in the case of Fe(CO)$_5$ + C$_3$H$_8$ pyrolysis, which
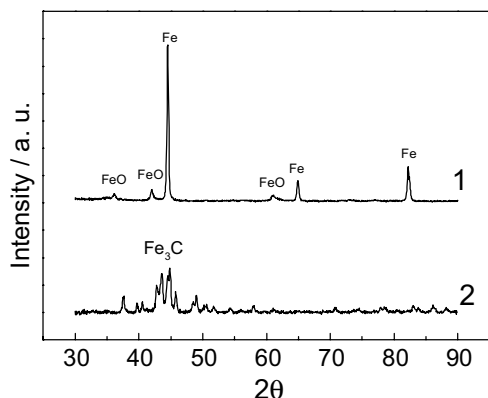
Figure 10. XRD patterns of the nanoparticles sampled at $T = 1173$ K: during Fe(CO)$_5$ pyrolysis (curve 1), the inlet molar fraction is [Fe(CO)$_5$]$_0$ = 1.1×10^{-4} and during Fe(CO)$_5$+C$_3$H$_8$ pyrolysis (curve 2), the inlet molar fractions are [Fe(CO)$_5$]$_0$ = 1.4×10^{-4} and [C$_3$H$_8$]$_0$ = 4.6×10^{-3}.
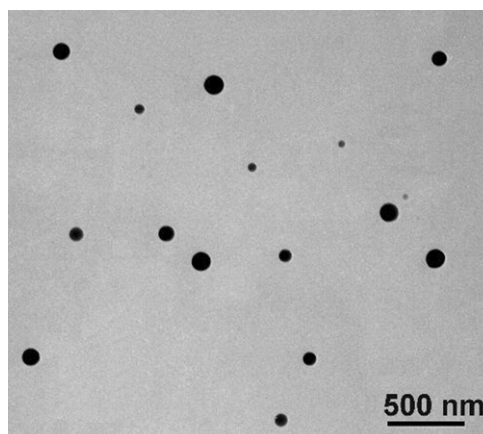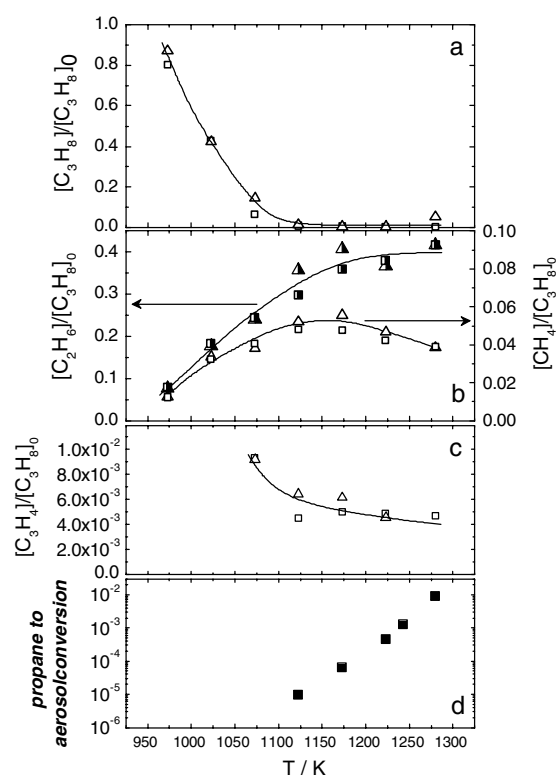

Figure 11. (*a*)–(*c*) The relative gaseous concentrations of propane (*a*) and intermediates (*b*) and (*c*) in the mixtures sampled at the outlet of reactor versus the pyrolysis temperature; (*d*) ratio of the outlet aerosol mass concentration to the inlet mass concentration of carbon as a constituent of C$_3$H$_8$. Triangular symbols correspond to the Ar+C$_3$H$_8$+Fe(CO)$_5$ mixture ([C$_3$H$_8$]$_0$ = 2.78×10^{-3}, [Fe(CO)$_5$]$_0$ = 2.8×10^{-5}) and squares to the Ar + C$_3$H$_8$ mixture ([C$_3$H$_8$]$_0$ = 1.34×10^{-3}).

is described in detail in the following section, yields evidence of the Fe$_3$C phase (figure 10 curve 2) in the aerosol particles.

3.2. Pyrolysis of C$_3$H$_8$+Ar and C$_3$H$_8$+Fe(CO)$_5$+Ar mixtures

Figures 11(*a*)–(*c*) show the concentrations of propane and gaseous intermediates at the outlet of the flow reactor as
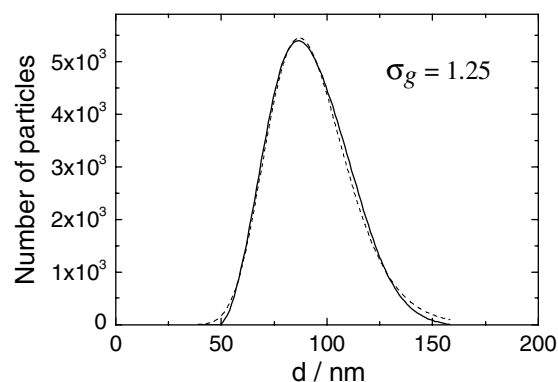

Figure 12. TEM images of soot nanoparticles formed during the pyrolysis of Ar+C$_3$H$_8$ mixture at $T = 1280$ K and inlet molar fraction [C$_3$H$_8$]$_0$ = 1.34×10^{-3}.

Figure 13. Size distribution of soot particles formed under pyrolysis of C$_3$H$_8$+Ar mixture. Solid line–ADB data; dotted line corresponds to log-normal function with the standard geometric deviation $\sigma_g = 1.25$, pyrolysis temperature $T = 1280$ K and inlet molar fraction is [C$_3$H$_8$]$_0$ = 1.34×10^{-3}.

a function of the pyrolysis temperature. It is possible to observe that the gaseous concentrations are almost identical in the two cases of C$_3$H$_8$+Ar and C$_3$H$_8$+Fe(CO)$_5$ + Ar. Preliminary pyrolysis of mixture propane plus argon C$_3$H$_8$+Ar is investigated. This process produces the formation of single spherical soot particles (figure 12) with typical size spectrum with the mode centred about 85 nm as measured by the ADB spectrometer and shown in figure 13. The size distribution is described well by the log-normal function with the standard geometric deviation $\sigma_g \approx 1.25$. Figure 14 shows the mean arithmetic radius of the soot particles and the particle number concentration at the reactor outlet versus the temperature of pyrolysis. Both particle radius and concentration are measured as increasing with increasing temperature. For comparison, figure 14(*a*) gives (square) the value of the mean particle radius as determined from TEM images elaboration which is in good agreement with the ADB data (circles). We used the data of figure 14 to evaluate the propane to aerosol conversion assuming the particle density to be about 2 g cm^{-3} (see figure 11(*d*)).

We focus then on the pyrolysis of mixture Ar diluted propane and iron pentacarbonyl. The crystalline structure and morphology of the aggregates formed by the pyrolysis
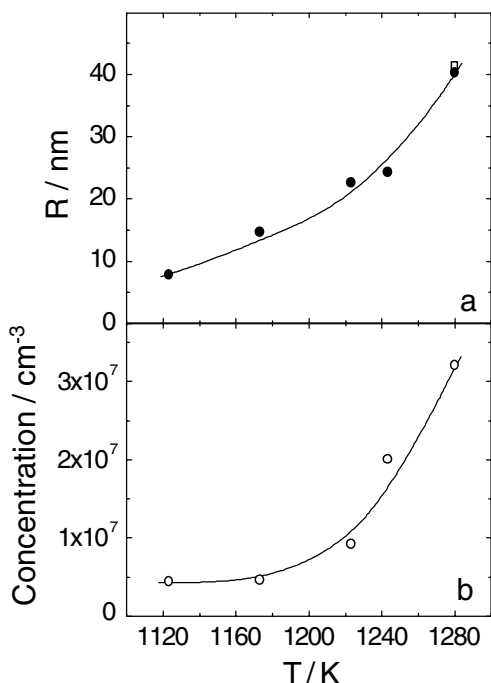
Figure 14. Mean arithmetic radius R (a) and number concentration (b) of soot nanoparticles as measured at the outlet of reactor (at room temperature) versus the pyrolysis temperature, inlet molar fraction is $[C_3H_8]_0 = 1.34 \times 10^{-3}$ (circles—-ADB data, square—-TEM data).

of $C_3H_8+Fe(CO)_5+Ar$ were analysed by the XRD method and TEM, respectively. For the inlet molar fraction ratio $[C_3H_8]_0/[Fe(CO)_5]_0$ being in the range from 2 to 40 with $T = 1173$ K, the single crystalline phase Fe_3C was observed in the XRD patterns (see the example shown above in figure 10, spectrum 2). The TEM analysis of aggregates produced by the pyrolysis of $C_3H_8+Fe(CO)_5+Ar$ showed that the aggregate morphology was weakly dependent on the initial molar fractions of $Fe(CO)_5$ and C_3H_8 in the range $[Fe(CO)_5]_0 = 8.2 \times 10^{-6}$–$1.4 \times 10^{-4}$, $[C_3H_8]_0 = 5.2 \times 10^{-4}$–$7.6 \times 10^{-3}$ ($T = 1173$ K) and was mainly determined by the initial ratio $[C_3H_8]_0/[Fe(CO)_5]_0$. In particular, corresponding to the range $[C_3H_8]_0/[Fe(CO)_5]_0$ below about 30 the aerosol aggregates were observed (figures 15(a)–(c) to be composed of Fe_3C particles covered by carbon. The diameter of Fe_3C particles was in the range 5–100 nm. Smaller Fe_3C particles were coated by amorphous carbon (figure 15(b)) whereas graphitized carbon was found to constitute the external shell of larger Fe_3C particles (figure 15(c)). In the range $[C_3H_8]_0/[Fe(CO)_5]_0 > 30$ carbon nanotubes were formed, thus the resulting structures consisted of small groups of particles connected by long single-wall and multi-wall nanotubes (figure 15(d)). The length and diameter of the carbon nanotubes depended on the inlet mixture composition and pyrolysis temperature. For example, the typical conditions for carbon nanotube formation were the temperature range $1073 < T < 1280$ K and the ratio of reagent concentrations
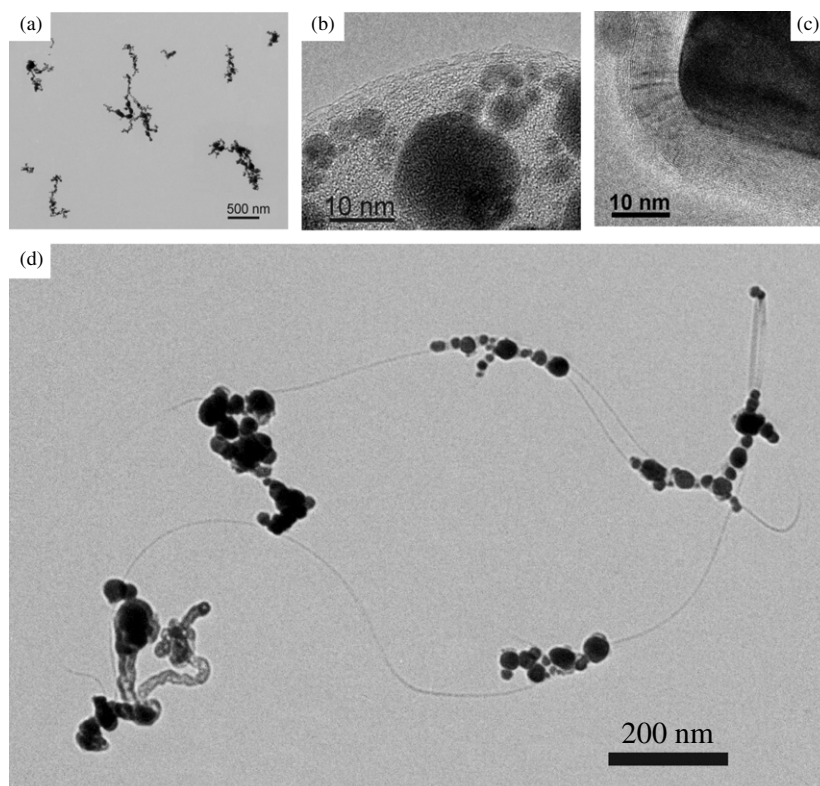

Figure 15. Examples of TEM and HRTEM images of Fe_3C covered by carbon (a,b,c) and complex aggregates (d) formed under co-pyrolysis of propane and $Fe(CO)_5$. Pyrolysis temperature $T = 1173$ K, inlet molar fractions $[C_3H_8]_0$ and $[Fe(CO)_5]_0$ are 1.25×10^{-3} and 1.052×10^{-4} (a,b,c) and 7.5×10^{-4} and 9.2×10^{-6} (d), respectively. (b) Small Fe_3C particles of aggregate covered by amorphous carbon shell; (c) large Fe_3C particle of aggregate coated by graphite-like shell.
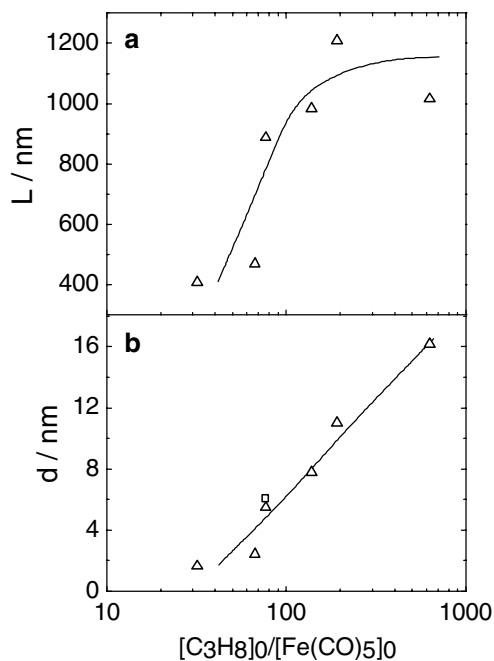
Figure 16. Mean arithmetic length (L) and diameter (d) of carbon nanotubes versus the ratio of inlet molar fraction $[C_3H_8]_0/[Fe(CO)_5]_0$, pyrolysis temperature $T = 1173$ K (triangles—TEM image elaboration; square symbol—HRTEM data).

$30 < [C_3H_8]_0/[Fe(CO)_5]_0 < 650$. Figure 16 shows the mean arithmetic diameter and length of carbon nanotubes versus the inlet propane to iron pentacarbonyl ratio of molar fractions. The mean diameter and the length of carbon nanotubes increase with the ratio $[C_3H_8]_0/[Fe(CO)_5]_0$. Results from TEM analysis were compared with some findings from HRTEM (square point in figure 16(*b*)) in order to check the reliability of assessment of the CNT mean arithmetic diameter. Accord was found and most of the analysis was performed on TEM observations. We used the fractal-like dimension approach to describe the morphology of complex aggregates composed of both particles and nanotubes using relationship (2) as was done before in the case of iron pentacarbonyl pyrolysis. The geometric radius was determined using equation (1). Figure 17 shows D_f versus the $[C_3H_8]_0/[Fe(CO)_5]_0$ ratio. D_f is observed to be decreasing with an increase in the ratio $[C_3H_8]_0/[Fe(CO)_5]_0$ from about 10 up to 80. This result is coherent with the finding discussed above about the increase in the mean nanotube length with the propane relative concentration (figure 16(*a*)). At higher ratios ($[C_3H_8]_0/[Fe(CO)_5]_0 > 80$) the fractal-like dimension increases with increasing $[C_3H_8]_0/[Fe(CO)_5]_0$ ratio. This result is in agreement with the fact that the mean nanotube length does not change with the propane relative concentration in this range, whereas the mean nanotube diameter increases monotonically (figure 16(*b*). HRTEM analysis showed that the complex aggregates contain a different kind of nanotubes including single-wall (figure 18) as well as multi-wall nanotubes (figures 19 and 20). At low ratios $[C_3H_8]_0/[Fe(CO)_5]_0 < 80$ single-wall nanotubes (SWNTs) dominated in the samples; in the range $80 < [C_3H_8]_0/[Fe(CO)_5]_0 < 140$ both SWNTs and bamboo-like nanotubes were present. At $[C_3H_8]_0/[Fe(CO)_5]_0 > 150$ the samples contained both bamboo-like and hollow MWNTs.

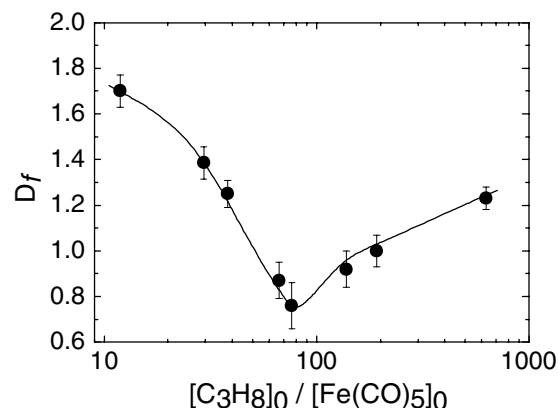**Figure 17.** Dependence of fractal-like dimension of complex aggregates on the inlet ratio $[C_3H_8]_0/[Fe(CO)_5]_0$; pyrolysis temperature $T = 1173$ K.
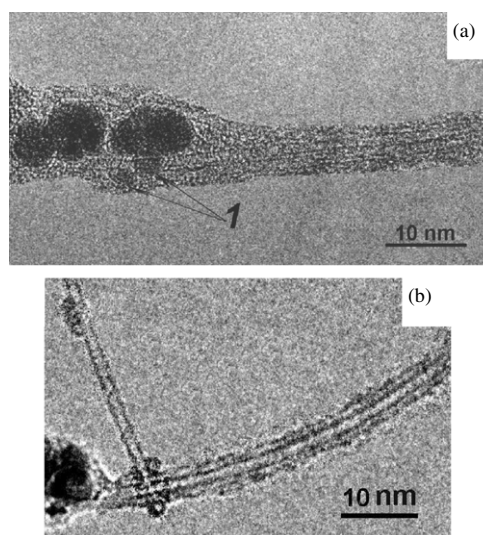

Figure 18. (*a*, *b*) HRTEM images of single-wall carbon nanotubes (SWNTs) formed by pyrolysis of $C_3H_8+Fe(CO)_5+Ar$ mixture. In part (*a*) the regions marked 1 are Fe_3C nanoparticles on basis of SWNTs. Pyrolysis temperature $T = 1173$ K, inlet molar fractions of reagents $[C3H8]_0$ and $[Fe(CO)_5]_0$ are 7.5×10^{-4} and 9.2×10^{-6}, respectively.

From the TEM images it is possible to evaluate the fraction of nanotubes, i.e. the average number of nanotubes per aggregate, as a ratio between the total number of nanotubes and the total number of aggregates in the sample. Actually, this ratio reflects the probability of nanotube nucleation during the reaction time. Figure 21(*a*) shows the nanotube fraction versus the ratio between the initial concentrations of C_3H_8 and $Fe(CO)_5$. One can see that at $[C_3H_8]_0/[Fe(CO)_5]_0 > 100$ the nanotube fraction is higher than unity, i.e. many aggregates are observed, which include more than one nanotube.

4. Discussion

4.1. Pyrolysis of Fe(CO)₅ + Ar mixture

It is important to know the temperature region in which the homogeneous decomposition dominates. The pentacarbonyl homogeneous decomposition can be described by the first
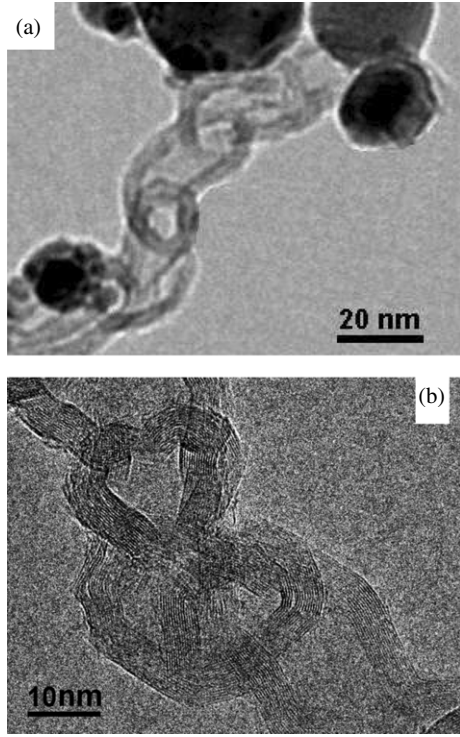
Figure 19. (*a*, *b*) HRTEM images of bamboo-like multi-wall carbon nanotubes (MWNTs). Pyrolysis temperature $T = 1173$ K, inlet molar fractions of reagents $[C_3H_8]_0$ and $[Fe(CO)_5]_0$ are 7.5×10^{-4} and 9.2×10^{-6}, respectively.

order kinetics via the expression

$$\frac{\Delta[Fe(CO)_5]_{HOM}}{[Fe(CO)_5]_0} = 1 - \exp(-k_{HOM}t) \qquad (4)$$

where $\Delta[Fe(CO)_5]_{HOM}$ represents the decrease in the iron pentacarbonyl concentration due to the homogeneous decomposition, t is the reaction time and k_{HOM} is the homogeneous decomposition rate constant [47]:

$$k_{HOM} = 5.01 \times 10^{15} \exp(-165458 \pm 9977(J\,mol^{-1})/RT)\,(s^{-1}). \qquad (5)$$

The solid line in figure 22 shows the prediction of the iron pentacarbonyl decomposition degree at the reactor outlet in the case that only the homogeneous decomposition contributes. The prediction of homogeneous decomposition is considerable at temperature $T > 500$ K.

Results summarized in figures 2–4 are now discussed in order to compare the contribution of the predicted homogeneous versus the measured heterogeneous decomposition. In particular, in figure 2 with correspondence to lower ($T < 500$ K) pyrolysis temperatures, the heterogeneous decomposition is found to dominate (see figure 2, which shows that the activated wall conversion is about 75% while that for non-activated walls is negligible) and the stationary ratio $[Fe(CO)_5]/[Fe(CO)_5]_0$ decreases with the inlet $Fe(CO)_5$ concentration increasing with temperature being kept constant (figure 4(*b*)). We found that the heterogeneous decomposition follows the second order kinetics:

$$\frac{[Fe(CO)_5]}{[Fe(CO)_5]_0} = (1 + k[Fe(CO)_5]_0 t)^{-1}. \qquad (6)$$
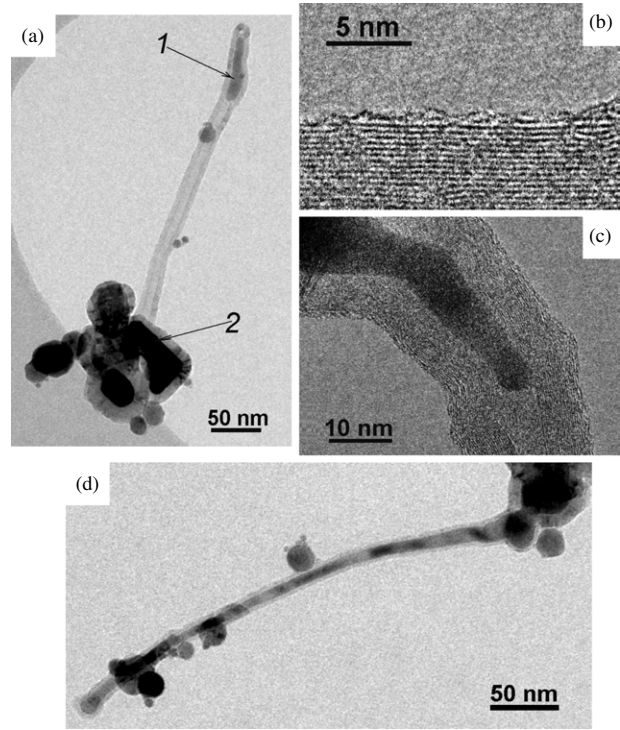

Figure 20. HRTEM images of multi-wall carbon nanotubes (MWNTs): (*a*) an example of hollow MWNT (1—drop-like particle, 2—particle on nanotube basis); (*b*) graphite layers of MWNT wall with a lattice parameter (d_{002}) 0.34 nm; (*c*)— nanotube fragment with Fe_3C drop-like particle; (*d*)—MWNT thick with Fe_3C. Pyrolysis temperature $T = 1173$ K, inlet molar fractions $[C_3H_8]_0$ and $[Fe(CO)_5]_0$ are 7.5×10^{-4} and 9.2×10^{-6}, respectively.

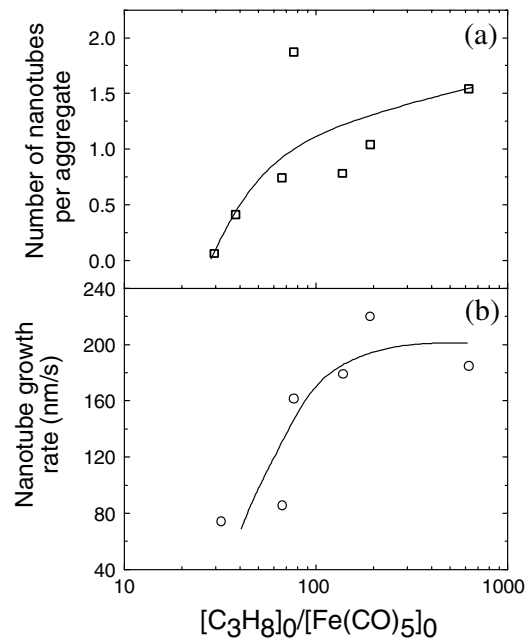**Figure 21.** The number of nanotubes per aggregate (*a*) and nanotube growth rate (*b*) as a function of the inlet ratio $[C_3H_8]_0/[Fe(CO)_5]_0$; pyrolysis temperature $T = 1173$ K.
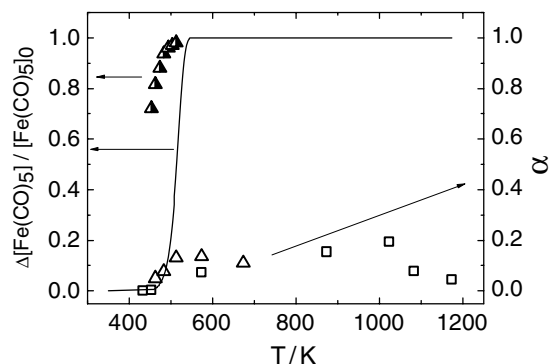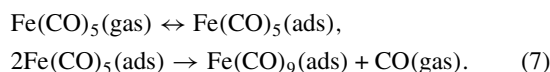
Figure 22. Temperature dependence of the iron pentacarbonyl decomposition degree and the ratio (α) of the outlet aerosol mass concentration to the iron mass concentration consistent with the inlet Fe(CO)$_5$. Solid line was calculated via equations (4) and (5). Semi-filled symbols—experimental data. Open symbols—evaluations from the values of aerosol number concentration and radius (see text). Inlet molar fractions [Fe(CO)$_5$]$_0$ = 6.5 × 10^{-6} (triangles), 9.5 × 10^{-5} (squares).

where k is the second order rate constant (see, figures 4(*b*) and 3). From the data shown in figure 3 the rate constant was determined as $k = 4.2 \times 10^{-15}\,\text{cm}^3\,\text{s}^{-1}$. It is reasonable to assume that the limiting stage is the surface dimerization:

$$\text{Fe(CO)}_5(\text{gas}) \leftrightarrow \text{Fe(CO)}_5(\text{ads}),$$
$$2\text{Fe(CO)}_5(\text{ads}) \rightarrow \text{Fe(CO)}_9(\text{ads}) + \text{CO(gas)}. \qquad (7)$$

The total Fe(CO)$_5$ conversion (as follows from figure 4) is presented in figure 22 with sphere symbols. It is interesting to compare the total conversion with the homogeneous decomposition degree and the efficiency α of conversion of Fe(CO)$_5$ with the aerosol particles. The efficiency α can be evaluated as the ratio between the outlet aerosol mass concentration and the inlet mass concentration of Fe which is a constituent of Fe(CO)$_5$. We evaluated the outlet aerosol mass concentration from the temperature dependences of aerosol number concentration and radius (figure 4) using equation (3). In the temperature range $T = 450\text{--}490\,\text{K}$ the aerosol conversion is approximately equal to the homogeneous decomposition degree, which means that aerosol particles are a product of homogeneous decomposition. At pyrolysis temperatures higher than 500 K aerosol conversion does not exceed 0.30 which is much less than the Fe(CO)$_5$ homogeneous decomposition degree. The discrepancy may be related to the heterogeneous loss of Fe(CO)$_5$ in the preheating zone (i.e. the inlet zone in the range 0–5 cm, see, figure 1).

4.2. Co-pyrolysis of C$_3$H$_8$+Fe(CO)$_5$ mixtures

Morphology evolution of complex aerosol aggregates has a more complicated character, with respect to the case of iron aerosol aggregates. Initial stages of aerosol formation depend essentially on the kinetics of the Fe(CO)$_5$ and propane decomposition. We can estimate the decomposition rate of these reagents in our experimental conditions. The rate constant of propane homogeneous decomposition was measured experimentally by different experimental groups for the typical propane pressures to be in the range 0.1–1 bar. These experimental constants are in good concordance with
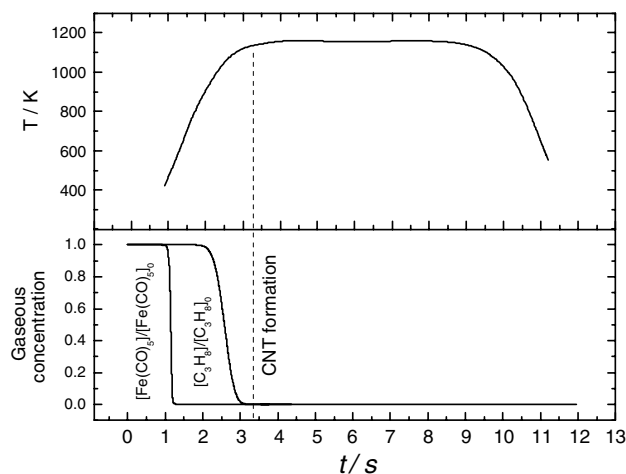
Figure 23. Scheme of particle evolution during pyrolysis of Fe(CO)$_5$ + C$_3$H$_8$ + Ar mixture at reaction temperature 1173 K and input flow rate 8 sccs.

the other [55–61]. The largest temperature range 1100–1400 K was covered by Benson [55] by the shock tube technique resulting in the first order rate constant expression:

$$k_{\text{C}_3\text{H}_8}^{\text{Benson}} = 1.27 \times 10^{12}\exp[(-234.5\,\text{kJ mole}^{-1})/RT](s^{-1}) \qquad (8)$$

Our measurements of this rate constant were done for the inlet propane pressure 1.1×10^{-3} bar, i.e. two orders of magnitude less than in the other authors' studies [55–61]. Thus, from the experimental data about propane decomposition, see figure 11(*a*), it is possible to infer the following first order rate constant:

$$k_{\text{C}_3\text{H}_8} = 9.13 \times 10^{10}\exp[-233.3(\text{kJ mole}^{-1})/RT]\,(s^{-1}), \qquad (9)$$

which is an order of magnitude less than Benson's value. At the pyrolysis temperature $T = 1073\,\text{K}$ the rate constants for Fe(CO)$_5$ and propane decomposition estimated via equations (5) and (9) are $4.4 \times 10^7\,\text{s}^{-1}$ and $0.4\,\text{s}^{-1}$, respectively. In other words, in our temperature range the Fe(CO)$_5$ decomposition rate was much higher than the propane decomposition rate. Thus, simple estimations show that the complete decomposition of Fe(CO)$_5$ occurs at the reactor input zone on reaching a temperature of about 500 K, while the propane begins to decompose later at 960 K (figure 11).

In order to draw a scheme to describe the process occurring in the flow reactor versus the residence time, the gas temperature and the concentrations of Fe(CO)$_5$ and C$_3$H$_8$ are shown as the reacting gases proceed inside the flow reactor (figure 23). The initial time corresponds to the reactor inlet point. The time-dependence of the gas temperature was recalculated from the experimental temperature profile (see, for example, figure 1) taking into account the gas temperature expansion coefficient. The gas concentration curves were calculated from equations (5) and (9). One can see that during the time 0–1.2 s iron pentacarbonyl decomposes completely, while the propane conversion is negligible. Thus, in the range 1.2–2.0 s the flow contains chain-like iron aggregates (because the temperature is less than the Curie point, see section 3.1). During the time 2.0–3.0 s propane decomposition occurs in

the temperature range 900–1120 K. The decomposition is accompanied by the intermediates' deposition on the Fe aggregate surface followed by the carbon diffusion to the iron particles. The diffusion process results in the formation of Fe–C solution [62, 63, 65]. The melting point for this solution is about 910 K [62–64], thus, actually, at $t > 2$ s the gas flow contains the liquid phase Fe–C particles. At the reaction time $t \approx 3.4$ s the carbon concentration reaches a critical value [63] which we estimated (see next paragraph) to be equal to 60 at.%. In correspondence with this critical concentration of carbon the nanotubes' nucleation starts [65] (nucleation probability at this moment is about 0.1 for the initial ratio $[Fe(CO)_5]_0/[C_3H_8]_0 = 100$). The carbon concentration in the Fe–C solution was estimated from the TEM and HRTEM images under the assumption that in the reactor hot zone the majority of the carbon atoms in the aggregates are constituents of the Fe–C solution phase. At the reactor outlet the Fe_3C phase is formed and the excess of carbon forms the graphite or amorphous shell [63]. The estimation of the total carbon content in sampled aerosol aggregates was provided by measuring the volumes of carbon shells and Fe_3C particles using the densities for carbon and Fe_3C $\rho_c = 2.0$ g cm^{-3} and $\rho_{Fe_3C} = 7.7$ g cm^{-3}. Our estimations of the carbon critical concentration are in reasonable agreement with the experimental observations of the carbon concentration in the liquid Fe–C particles 50 at.% at $T = 910$–970 K [62–64]. At time $t > 3.4$ s both single-wall and multi wall nanotubes grow, while liquid Fe–C solution penetrates inside the MWNTs (see figures 20(a), (c), (d). The growth of nanotubes has the effect to disrupting the Fe–C aggregates resulting in small Fe–C fragments connected by relatively long nanotubes' segments (figure 15(d)).

5. Conclusions

In the case of pyrolysis of the $Fe(CO)_5$+Ar mixture the iron aggregate morphology depends essentially on the reaction temperature. In correspondence with relatively low temperatures (T about 450 K) the primary particle mean diameter is about 10 nm from the TEM analysis. Consequently, the primary particles are mostly superparamagnetic and they form rather compact aggregates with relatively large fractal dimensions (D_f about 1.7). At intermediate temperatures in the range 800 to 1000 K the primary particle diameter from TEM is 20 to 30 nm, and the majority of the particles behave according to ferromagnetic properties. Thus, open chain-like aggregates are formed in this case with fractal dimension D_f of about 1.2. In correspondence with reaction temperatures higher with respect to the Curie point (1043 K), the aggregates observed are rather compact again (D_f about 1.7 to 1.8).

In the case of pyrolysis of the C_3H_8+Ar and C_3H_8+Fe(CO)$_5$+Ar mixtures the propane decomposition rate constant was experimentally determined as $k_{C_3H_8} = 9.13 \times 10^{10} \exp[-233.3(\text{kJ mole}^{-1})/RT]$ (s^{-1}), which signifies an order of magnitude less than the literature data. This discrepancy is probably related to the fact that the propane concentrations used in this work were two orders of magnitude less with respect to the other literature studies.

It was found that in the case of C_3H_8+Fe(CO)$_5$+Ar mixture pyrolysis complex aggregates composed of Fe_3C particles connected by long nanotubes are formed. The aggregate morphology is a function of the inlet $[C_3H_8]_0/[Fe(CO)_5]_0$ ratio. In the range $10 < [C_3H_8]_0/[Fe(CO)_5]_0 < 80$, the aggregate fractal dimension D_f decreases from 1.7 to 0.8 with $[C_3H_8]_0/[Fe(CO)_5]_0$ decreasing, which is related to the increase in the nanotube mean length. Vice versa, in the case of the $[C_3H_8]_0/[Fe(CO)_5]_0$ ratio increasing above 80, the aggregate fractal dimension D_f is observed to rise again, which can be interpreted as the net result of the increase in the nanotube mean diameter corresponding to a relatively larger propane concentration.

References

[1] Longwell J P 1982 *Proc. 19th Symp. (Int.) on Combustion (The Combustion Institute, Pittsburg)* p 1339
[2] Zimmer A T 2002 *J. Environ. Monit.* **4** 628
[3] Goss K-U and Eisenreich S J 1997 *Atmos. Environ.* **31** 2827
[4] Koshland C P 1996 *Proc. 26th Symp. (Int.) on Combustion (The Combustion Institute, Pittsburg)* p 2049
[5] Nemmar A, Hoet P H M and Vanquickenborne B 2002 *Circulation* **105** 411
[6] Colbeck I, Appleby L, Hardman E J and Harrison R M 1990 *J. Aerosol. Sci.* **21** 527
[7] di Stasio S 2001 *J. Aerosol. Sci.* **21** 509
[8] Richter R, Sander L M and Cheng Z 1984 *J. Colloid Interface Sci.* **100** 203
[9] Hurd A J and Flower W L 1988 *J. Colloid Interface Sci.* **122** 178–92
[10] Onischuk A A *et al* 2003 *J. Aerosol. Sci.* **34** 383
[11] Vander Wal R L and Hall L J 2001 *Chem. Phys. Lett.* **349** 178
[12] Vander Wal R L and Ticich T M 2001 *Chem. Phys. Lett.* **336** 24
[13] Vander Wal R L, Ticich T M and Curtis V E 2000 *Chem. Phys. Lett.* **323** 217
[14] Le Q T, Schouler M C, Garden J and Gadelle P 1999 *Carbon* **37** 505
[15] Glerup M, Kanzow H, Almairac R, Castignolles M and Bernier P 2003 *Chem. Phys. Lett.* **377** 293
[16] Bladh K, Falk L K L and Rohmund F 2000 *Appl. Phys. A: Mater. Sci. Process.* **70** 317
[17] Hoenlein W, Kreupl F, Duesberg G S, Graham A P, Liebau M, Seidel R and Unger E 2003 *Mater. Sci. Eng.* C **23** 633
[18] Bernholc J, Brenner D, Buongiorno Nardelli M, Meunier V and Roland C 2002 *Annu. Rev. Mater. Res.* **32** 347
[19] Dresselhaus M S, Dresselhaus G and Jorio A 2004 *Ann. Rev. Mater. Res.* **34** 247
[20] Awasthi K, Srivastava A and Srivastava O N 2005 *J. Nanosci. Nanotechnol.* **5** 1616
[21] Lam C-W, James J T, McCluskey R and Hunter R 2004 *Toxicol. Sci.* **77** 126
[22] Maynard A D, Baron P A, Shvedova A A, Kisin E R and Catranva V 2004 *J. Toxicol. and Environ. Health* **67** 87
[23] Donaldson K, Aitken R, Tran L, Stone V, Duffin R, Forrest G and Alexander A 2006 *Toxicol. Sci.* **92** 5

[24] Shvedova A A *et al* 2005 *Am. J. Physiol. Lung Cell Mol. Physiol.* **289** L698

[25] Warheit D B, Laurence B R, Reed K L, Roach D H, Reynolds G A and Webb T R 2004 *Toxicol. Sci.* **77** 117

[26] Jia G *et al* 2005 *Environ. Sci. Technol.* **39** 1378

[27] Monteiro-Riviere N A, Nemanich R J, Inman A O, Wang Y Y and Riviere J E 2005 *Toxicol. Lett.* **155** 377

[28] Bottini M, Bruckner S, Nika K, Bottini N, Bellucci S, Magrini A, Bergamaschi A and Mustelin T 2006 *Toxicol. Lett.* **160** 121

[29] Manna S K, Sarkar S, Barr J, Wise K, Barrera E V, Jejelowo O, Rice-Ficht A C and Ramesh G T 2005 *Nano Lett.* **5** 1676

[30] Rummunger M D, Reinelt D, Babushok V and Linteris G T 1999 *Combust. Flames* **116** 207

[31] Reinelt D and Linteris G T 1996 *26th Int. Symp. on Combustion (Naples, Italy) (The Combustion Institute)* p 1421

[32] Beischer D and Winkel A 1937 *Naturwissenschaften* **26/27** 420

[33] Kasper G, Show S-N and Shaw D T 1980 *J. Am. Indust. Hyg. Assoc.* **41** 288

[34] Kasper G 1982 *Aerosol. Sci. Technol.* **1** 201

[35] Kasper G and Shaw D T 1983 *Aerosol. Sci. Technol.* **2** 369

[36] Kasper G and Wen H Y 1984 *Aerosol. Sci. and Technol.* 405

[37] Veintemillas-Verdaguer S, Bomati O and Morales M P 2003 *Mater. Lett.* **57** 1184

[38] Orthner H R and Roth P 2002 *Mater. Chem. Phys.* **78** 453

[39] Mavliev R A and Ankilov A N 1985 *Colloidny J. (Russ.)* **15** 523

[40] Mavliev R A, Ankilov A N and Baklanov A M 1984 *Colloidny J. (Russ.)* **46** 1136

[41] Ankilov A, Baklanov A, Mavliev R and Eremenko S 1991 *J. Aerosol. Sci.* **22** S325

[42] Samson R J, Mulholland G W and Gentry J W 1987 *Langmuir* **3** 272

[43] Friedlander S K 2000 *Smoke, Dust and Haze* (Oxford: Oxford University Press)

[44] Rogak S N, Baltensperger U and Flagan R C 1991 *Aerosol. Sci. Technol.* **14** 447

[45] Powder Diffraction File No 06-0696, International Center for Diffraction Data, 12 Campus Boulevard, Newton Square, PA 19073-2373, USA

[46] Zhao X Q, Liu B X, Liang Y and Hu Z Q 1996 *J. Magn. Res. Magn. Mater.* **164** 401

[47] Lewis K E, Golden D M and Smith G P 1984 *J. Am. Chem. Soc.* **106** 3905

[48] Wasilevski P J 1981 *Shock Waves and High Strain Rate Phenomena in Metals* (New York: Plenum) 779

[49] Meakin P 1984 *Phys. Rev.* A **29** 997

[50] Raymond F, Mountain D, George W, Mulholland W and Baum H 1986 *J. Colloid Interface Sci.* **114** 67

[51] Witten T A and Sander L M 1981 *Phys. Rev. Lett.* **47** 1400

[52] Nubold H *et al* 2003 *Icarus* **165** 195

[53] Niklasson G A *et al* 1988 *Phys. Rev. Lett.* **60** 1735

[54] Helgesen G *et al* 1988 *Phys. Rev. Lett.* **61** 1736

[55] Benson A M 1967 *AIChE J.* **13** 903

[56] Bakh G, Novak Z, Korochuk S I and Kalinenko R A 1974 *Kinet. Catal.* **15** 1103

[57] Zychlinski W, Bach G, Heinrich K and Zimmermann G 1979 *Chem. Technol. (Leipzig)* **31** 1191

[58] Kalinenko R A *et al* 1983 *Kinet. Catal.* **24** 1031

[59] Laidler K J, Sagert N H and Wojciechowski B W 1962 *Proc. R. Soc. Lond.* **270** 254

[60] Jezequel J Y, Baronnet F and Niclause M 1983 *J. Chim. Phys.* **80** 455

[61] Marek L F and Cluer W B 1931 *Indust. Eng. Chem.* **23** 878

[62] Krivoruchko O P, Maksimova N I, Zaikovski V I and Salanov A N 2000 *Carbon* **38** 1075

[63] Krivoruchko O P and Zaikovski V I 1998 *Kinet. Catal.* **39** 607

[64] Parmon V N 1996 *Catal. Lett.* **42** 195

[65] Maksimova N I, Krivoruchko O P, Mestl G, Zaikovskii V I, Chuvilin A L, Salanov A N and Burgina E B 2000 *J. Mol. Catal. A: Chem.* **158** 301